JOURNAL OF MATERIALS SCIENCE 21 (1986) 3873–3883

Ordered domain characterization in α-Cu–Al alloys from dissolution kinetics studies

ARI VARSCHAVSKY, EDUARDO DONOSO
Universidad de Chile, Facultad de Ciencias Físicas y Matemáticas, Instituto de Investigaciones y Ensayes de Materiales (IDIEM), Casilla 1420, Santiago, Chille

Through microcalorimetric experiments, disperse order (DO) dissolution kinetics in pre-annealed α-Cu–Al alloys containing 19, 13 and 6.5 at% aluminium were adequately described by the integrated kinetic model function arising from the steady-state part of the diffusion field: $f(y) = 1 - (1 - y)^{2/3}$. Domain sizes after the annealing treatment, and also critical radii, were determined from differential scanning calorimetry data analysis at different heating rates. The existence of critical radii indicates that the disperse-order dissolution process is a first-order transition. Nevertheless, it was inferred that for very dilute alloys, only short-range order is present. After pre-annealing the alloys at different temperatures, volume fractions and domain concentrations were computed by employing the above kinetic model under high heating-rate conditions. On the basis of appropriate time constant and diffusion time calculations, the range of such temperatures compatible with equilibrium attainment was established. Prolonged pre-anneals alter the particle distribution, but do not influence either volume fractions or domain sizes. A semi-quantitative particle radius–particle concentration–temperature diagram was proposed for α-Cu–Al alloys.

1. Introduction

Differential scanning calorimetry (DSC) has been shown to be an appropriate technique for research on annealing and ageing phenomena in metals and alloys [1–6], not only because of its simple and straightforward application, but mainly because the measured quantity (a heat effect) is directly connected with the process under investigation, in comparison with other methods which in general may give only a rather indirect indication for most solid-state processes. Evolution or absorption of heat takes place in such processes and can be detected before the changes in structure (ordered domains, precipitates, etc.) relating to it become observable by other means. The way in which this energy is released or absorbed has also been proved to be quite sensitive to non-localized variations in particle type, size and volume fraction [7, 8]. In addition, information concerning the reaction kinetics is supplied by the thermograms. Several reviews are available [9–11].

Based on the theory of precipitate dissolution kinetics proposed by Whelan [12], expressions suitable for use under non-isothermal conditions have been derived [13]. Such expressions indicate that additional structure information, particularly particle size data, may be obtainable from the kinetic analysis of dissolution reactions in DSC, and that the form of the appropriate kinetic model function is strongly influenced by the particle shape.

The purpose of this paper is to present a study on the dissolution kinetics of disperse ordered domains in α-Cu–Al alloys, focused mainly on the determination of particle sizes and concentration during linear heating-rate experiments. Also the attainment of equilibrium will be explored, and a particle size–domain concentration–temperature–alloy composition representation will be made. These alloys were chosen for this study, since their behaviour has been documented in previous publications [14–25] on the basis of thermal analysis results.

2. Theoretical considerations

The starting point to the usual approach to non-isothermal kinetics is a general relationship between the dimensionless parameter, y, which measures the extent of the reaction, the reaction rate coefficient, $k(T)$, and the time, t:

$$f(y) = k(T)\,t \tag{1}$$

In Equation 1, $f(y)$ is designated as the associated integrated kinetic function. Assuming that the rate coefficient obeys an Arrhenius equation, and that the heating rate, $\alpha = \mathrm{d}T/\mathrm{d}t$, is constant, the following equation holds under non-isothermal conditions [10]:

$$f(y) = (AE/R\alpha)p(x) \tag{2}$$

where A is the pre-exponential term in the Arrhenius equation, E the activation energy and R the gas constant. The function $p(x)$, where $x = E/RT$, is a definite integral which can be accurately approximated by several expressions [26] among them:

$$p(x) = (x + 2)^{-1}x^{-1}\exp(-x) \tag{3}$$

if the three-dimensional Schlomilch expression [27] is used.

Although the form of $f(y)$ is non-restricted on a phenomenological basis, physical justification is desired when selecting the appropriate expression,

0022–2461/86 $03.00 + .12

because more reliable adjusted parameters could be expected.

A non-isothermal precipitate dissolution kinetics approach has already been given in an earlier paper [17]. Therefore only a brief summary will be made here.

From the relationships giving the concentration profile and the flux of the solute at the interface of a dissolving spherical precipitate of radius r at time t [12, 28], the following differential equation is obtained for the instantaneous radius of the precipitate:

$$\frac{dr}{dt} = -\frac{kD}{2r} - \frac{k}{2}\left(\frac{D}{\pi t}\right)^{1/2} \quad (4)$$

where D is the volume diffusion coefficient in the matrix and $k = 2(c_i - c_M)/(c_p - c_i)$; c_i is the concentration in the matrix at the precipitate–matrix interface, c_M is the solute concentration of the matrix and c_p is the composition of the precipitate. For planar interfaces, the term r^{-1} which arises from the steady-state part of the diffusion field [12] does not contribute to the rate of dissolution; hence Equation 4 integrates under isothermal conditions to

$$r = r_0 - (Dt/\pi)^{1/2} \quad (5)$$

where r_0 is the initial half-thickness of the precipitate. If the term $t^{-1/2}$, which arises from the transient part of the diffusion field [12], is neglected (e.g. for long times), solution of Equation 4 yields

$$r^2 = r_0^2 - kDt \quad (6)$$

where r_0 is the initial precipitate radius in this case. Transformation of Equations 5 and 6 into suitable expressions for kinetic analysis in terms of y, which is related to the instantaneous and initial precipitate volume fractions V_f and V_0, respectively, requires that

$$y = 1 - (V_f/V_0) = 1 - (r/r_0)^3 \quad (7)$$

From Equations 5 and 7, one gets

$$[1 - (1 - y)^{1/3}]^2 = K_1 t/r_0^2 \quad (8)$$

in which K_1/r_0^2 is the equivalent rate constant and $K_1 = k^2D/\pi$. If one assumes that the temperature dependence of the reaction rate constant follows an Arrhenius equation, as may be expected from the major dependence of the rate on the diffusion coefficient, by employing the usual approaches to non-isothermal kinetics one finds that Equation 8 becomes

$$[1 - (1 - y)^{1/3}]^2 = (EA_1/R\alpha r_0^2)\, p(x) \quad (9)$$

where A_1 is a constant. This equation describes essentially one-dimensional diffusion situations [13]. Also, from Equations 6 and 7, a rate equation which describes essentially three-dimensional diffusion-controlled situations is [13]

$$1 - (1 - y)^{2/3} = K_2 t/r_0^2 \quad (10)$$

where $K_2 = kD$. By the same developments as those given earlier, under non-isothermal condition Equation 10 becomes

$$1 - (1 - y)^{2/3} = (EA_2/R\alpha r_0^2)\, p(x) \quad (11)$$

where A_2 is a constant.

Only the integrated kinetic functions, $f(y)$, such as those presented in Equations 9 and 11 which were developed on the basis of a physical model for the dissolution process, lead to pre-exponential factors proportional to r_2^{-2} ($A = A_1 r_0^{-2}$ or $A = A_2 r_0^{-2}$ in Equation 2), depending upon the precipitate shape: planar or spherical, respectively.

3. Materials and experimental methods

The three α-Cu–Al alloys studied contained, respectively, 3.00 ± 0.04, 6.00 ± 0.07 and 9.0 ± 0.10 wt % Al (99.97 wt %). They were prepared in a Baltzer VSG 10 vacuum induction furnace from electrolytic copper (99.95 wt %) in a graphite crucible. The ingots were subsequently forged at 923 K to a thickness of 10 mm, pickled with a solution of nitric acid (15%) in distilled water to remove surface oxide, annealed in a vacuum furnace at 1123 K for 36 h to achieve complete homogeneity, and cooled in the furnace to room temperature. They were cold-rolled to 1.5 mm thickness with intermediate annealing periods at 923 K for one hour. After the last anneal the material was finally rolled to 0.75 mm thickness (50% reduction). A subsequent heat treatment was performed at 723 K for one hour, after which the alloys were furnace-cooled at a rate of 15 K h^{-1} and subsequently pre-annealed at 470 K for 80 h.

Microcalorimetric analysis of the samples was performed in a Dupont 990 Thermal Analyser. Specimen discs of 0.75 mm thickness × 6 mm diameter were prepared for each material condition. DSC measurements of the heat flow were made by operating the calorimeter in the constant-heating mode (heating rates of 0.83, 0.67, 0.33, 0.17, 0.083 and 0.033 K sec^{-1} for the pre-annealed alloys, and 0.83 K sec^{-1} for the quenched material). Runs were made from room temperature to 740 K. To increase the sensitivity of the measurements a high purity, well annealed copper disc of approximately equal mass, in which no thermal events occur over the range of temperatures scanned, was used as a reference. In order to minimize oxidation, dried nitrogen (0.8×10^{-4} $m^3 min^{-1}$) was passed through the calorimeter. After each run, the data were converted to differential heat capacity against temperature, using a previously established calibration for the DSC cell. Subsequently a linear baseline was subtracted from the data. This baseline represents the temperature-dependent heat capacity of the copper–aluminum solid solutions and the existing ordered domains, and its value was in agreement with the Kopp–Neumann rule. The remainder, namely the differential heat capacity ΔC_p, represents the heat associated with the solid-state reactions which take place during the DSC run. Thus, the reaction peaks in the ΔC_p against T curves can be characterized by a reaction enthalpy of a particular event.

Thin foils suitable for transmission electron microscopy were prepared by cutting sheets in a Servomet spark-cutter machine. The sheets were electrolytically thinned to a thickness of 0.06 mm using a 50% phosphoric acid and 50% ethyl alcohol solution. Then, discs were shaped from the sheets in the spark-cutter machine by using a special holder developed in our

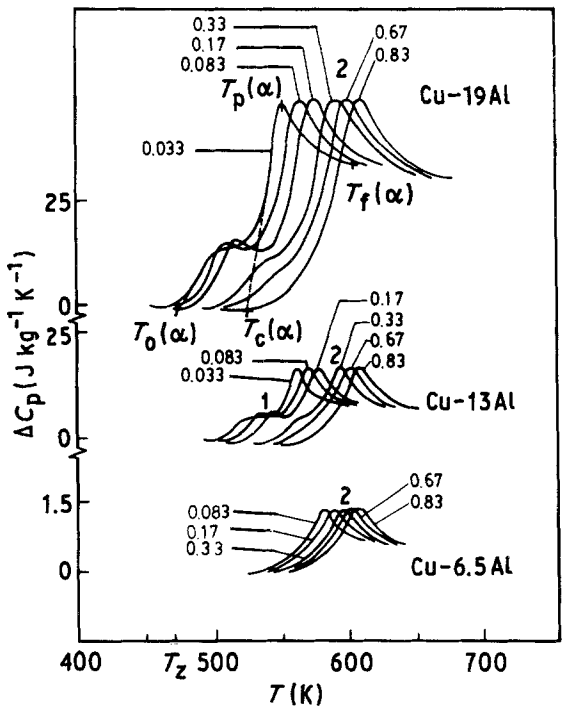

Figure 1 DSC thermograms for α-Cu–Al alloys furnace-cooled at 15 K h^{-1} and subsequently pre-annealed at 470 K for 80 H. Each curve is labelled with the heating rate α (K sec^{-1}).

laboratory [29], prior to the final electrolytic thinning in a Stuerss Tenupol machine using the same solution as above. Transmission electron microscopy was done in a Philips EM-300 electron microscope.

4. Results and discussion

4.1. DSC thermograms

Typical thermograms for the three alloys (pre-annealed at 470 K for 80 h), obtained from rising temperature experiments at the indicated heating rates α, are shown in Fig. 1. They are characterized by two endothermic peaks, namely Stages 1 and 2. It can be noticed that the onset temperature of Stage 1, $T_0(\alpha)$, increases with the heating rate, and for $\alpha = 0.83$ K sec^{-1} it does not appear at all. The shape of the trace changes from a large knee to a small peak, as α becomes larger. Simultaneously, the peak temperature, $T_{p1}(\alpha)$, shifts to larger values and the peak height increases. Nevertheless, as these effects become more conspicuous, the peak tends to be suppressed during Stage 2. It is also noticeable that Stage 1 shifts to higher temperatures as the aluminium content decreases.

The region of the thermograms associated with Stage 2 can be described by an endothermic peak whose onset temperature, $T_c(\alpha)$, peak temperature, $T_{p2}(\alpha)$ and ending temperature, $T_f(\alpha)$, shift to higher values with increasing heating rate. The height of this peak decreases as the heating rate does, looking at the same time sharper, and also $d(\Delta C_p)/dT$ becomes larger at the left inflection point. Besides, ΔC_p approaches a constant value after the reaction goes to completion. Similarly to Stage 1, it can be observed that the magnitude of Stage 2 decreases with the aluminium content and simultaneously shifts to higher temperatures. It is worthwhile to notice that both reactions are strongly interdependent. In fact, one can observe that the magnitudes of the processes involved in both reactions are opposed to each other.

Enthalpimetric analysis of DSC traces [25] pointed straightforwardly to interpreting both stages in terms of a disperse order (DO) mode. This state is characterized by the presence of highly ordered particles embedded in a disordered matrix. The unlimited coarsening of these particles is inhibited by coherency stresses, and equilibrium values exist for the volume fraction and also for the number of these regions depending on temperature [30]. Stage 1 is attributable to the adjustment of the domain volume fraction, V, and concentration, N, to equilibrium from a "frozen in" state, and Stage 2 can be associated with disperse-order dissolution [25].

Therefore in the following, the kinetic analysis of Stage 2 will be performed, according to the procedures described in Section 2.

4.2. Kinetic analysis

Before establishing the integrated kinetic function which adjusts better to the experimental data obtained from the DSC traces, it is necessary to point out that if the dissolved fraction of DO is y at time t, in DSC, $dy/dt = (1/A_0)(da_t/dt)$, where da_t/dt is the rate of heat flow, a_t is the area under the peak at time t, and A_0 is the total area under the peak. Values of the activation energies are also required as a necessary input in order to perform the non-isothermal kinetic analysis. These values were computed using the Kissinger method [31], which consist in determining the slope $(-E/R)$ of the straight line resulting when $\ln(\alpha/T_p^2)$ is plotted against $1/T_p$. The corresponding lines, which are shown in Fig. 2, give 146/151/171 kJ mol^{-1} for 19/13/6.5 at % Al alloys. These values agree reasonably well with those for self-diffusion reported in the literature [32–36].

The next step consists in adjusting to the experimental y $(= a_t/A_0)$ against T curves Equations 9 and 11, and also the simple first-order kinetic law

$$\ln(1 - y)^{-1} = (EA_3/R\alpha)p(x) \qquad (12)$$

(where $A = A_3$) in order to determine A for each case. Although this last integrated kinetic function has little physical justification for describing the dissolution behaviour of second-phase precipitates [13], it is useful for estimating relaxation times solely on a phenomenological basis. The calculated and experimental curves for $\alpha = 0.83$ K sec^{-1} are shown in Fig. 3. One can observe that both Equations 11 and 12 fit equally well to the experimental plots using the above computed values for E by adjusting A. These last values are listed in Table I.

Nevertheless, by the preceding argument, Equation 11 seems appropriate to be considered in the following, as it was developed on the basis of a physical model for the dissolution process and also can be used simultaneously to compute domain size. However, before accomplishing this objective, a complementary check of the above results under isothermal conditions was made at least for a Cu–19 at % Al alloy. A sample was heated at 5 K sec^{-1} to 10 K below its critical

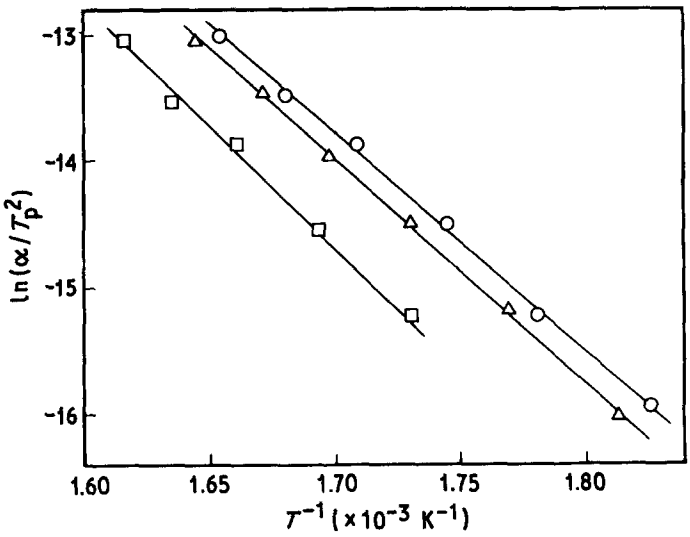

Figure 2 Kissinger plots for the variation of the temperatures corresponding to the maximum of the dissolution peaks as a function of the scan rate. (○) Cu–19Al, (△) Cu–13Al, (□) Cu–6.5Al.

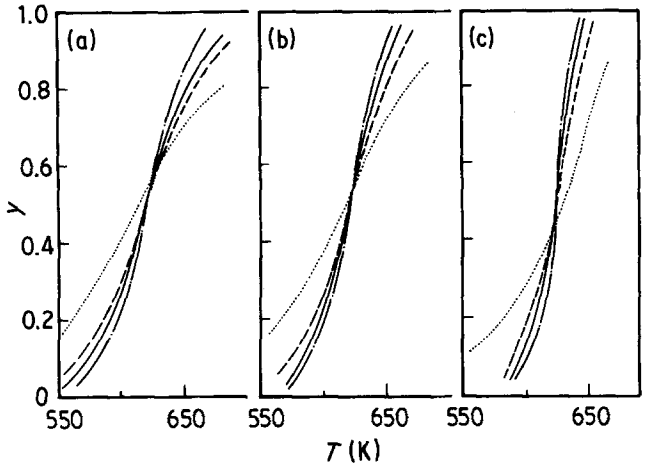

Figure 3 Experimental (——) and calculated y against T curves for disperse-order dissolution: (· · ·) Equation 9; (- - - -) Equation 11 and (- · - · -) Equation 12. (a) Cu–19Al, (b) Cu–13Al, (c) Cu–6.5Al.

temperature, T_c = 520 K [25], held for 1 min, then heated at 5 K sec^{-1} to the hold temperature, 573 K. The pause at (T_c − 10) K serves to reduce in part the transient effects due to thermal lags in DSC. The 573 K isothermal transformation trace is shown in Fig. 4. Since in the DSC isothermal mode the deflection from the baseline is directly proportional to the rate of reaction dy/dt at that instant, the corresponding y against t plots can readily be obtained. In Fig. 5 the experimental and calculated curves are shown. For such computations, the same values of E and A already determined were used, previously rewriting Equations 9, 11 and 12 in for the form of Equation 1 by setting $k(T) = A \exp(-E/RT)$. Again, it can be observed that the integrated kinetic functions $\ln(1-y)^{-1}$ and $1-(1-y)^{2/3}$ adjust better to the experimental curve. Therefore, it is justified to use this last function to determine particle sizes from non-isothermal kinetic data.

TABLE I Values for A adjusted to different kinetic laws*

Al (at %)	Equation 9 ($\times 10^{10}$ sec^{-1})	Equation 11 ($\times 10^{10}$ sec^{-1})	Equation 12 ($\times 10^{11}$ sec^{-1})
19	1.4 ± 0.1	4.6 ± 0.5	1.4 ± 0.1
13	4.3 ± 0.4	14 ± 2	4.2 ± 0.4
6.5	20 ± 2	64 ± 6	25 ± 3

*Data represent the average of 5 runs.

4.3. Domain size determination

From the analysis performed in the preceding section, it can be inferred that a plot of $f(y)$ against $p(x)$ adjusted to the experimental data using Equation 11 would lead to straight lines, actually shown in Fig. 6, of slope

$$m = EA_2/R\alpha r_0^2 \qquad (13)$$

Here r_0 is the domain radius at the onset of the non-isothermal dissolution process, which in turn depends on α. This procedure has been preferred to determine r_0 instead of fitting calculated to experimental y against T curves, once A_2 has been computed, because of the improvement in accuracy arising from linearization. Nevertheless, for identifying integrated kinetic

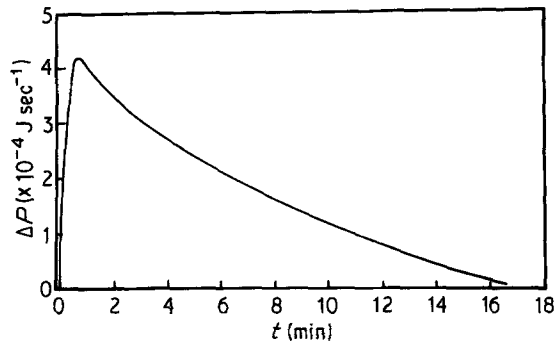

Figure 4 A DSC output for isothermal particle dissolution. Cu–19Al, T = 573 K.

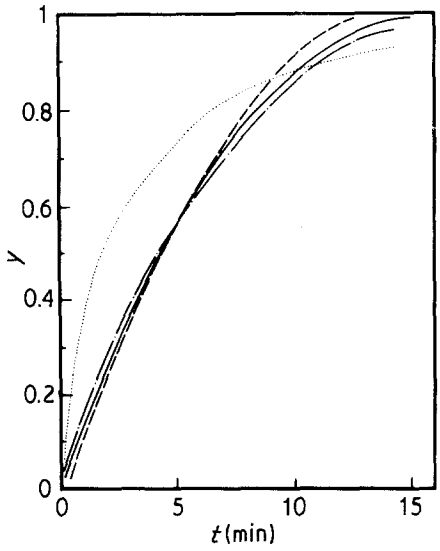

Figure 5 Experimental (——) and calculated y against t curves for disperse-order dissolution: (····) Equation 8, (----) Equation 10, (-·-·-) first-order kinetic law. Cu–19Al, $T = 573$ K.

functions the latter procedure proved more sensitive, presumably because y against T curves directly reflect DSC traces. Since the corresponding values of A ($= A_2/r_0^2$) are available (Table I), a measured value for r_0 by transmission electron microscopy allows one to calculate A_2. Fig. 7 is a dark-field TEM micrograph of a Cu–19 at % Al alloy furnace-cooled at 15 K h^{-1} and pre-annealed at 470 K for 80 h. Spherical particles can be observed, thus supporting the choice of Equation 11 to describe the dissolution behaviour. An average value of $r_0 = 13.0$ nm was measured on the micrograph by counting about 80 domains, giving $A_2 = 7.8 \times 10^{-6}$ m^2 sec^{-1} for this alloy.

The compositional dependence of A_2 can be explored on an experimental basis by making use of the electron microscopic study performed by Gaudig and Warlimont [35] at room temperature. They obtained values for r_0 of 10 and 5 nm for alloys containing 15 and 10 at % Al, respectively, while $N = 6 \times 10^{22}$ m^{-3} was the same for both alloys (cooled at 5.5 K h^{-1}). The temperature θ_0 at which the volume fraction of the Cu–15Al alloy becomes metastable at the above cooling rate can be obtained from the Bragg

Figure 7 Dark-field TEM micrograph for Cu–19Al, selected from a superlattice reflection. Zone [1 1 0].

and Williams estimation [36]:

$$E/R\theta_0 = \ln (R\theta_0^2/\alpha\tau_0 E) \qquad (14)$$

where $E = 151$ kJ mol^{-1} and $\tau_0 = 2.06 \times 10^{-13}$ sec, according to the processed data from Trieb and Veith [25]. A value of $\theta_0 = 476$ K was obtained. On the other hand, a pre-anneal at 470 K during 80 h after cooling the same alloy at a rate of 15 K h^{-1} corresponds to an equilibrium state of V at 471 K [25]. Therefore, within the approximations involved in the derivation of Equation 14, it can be inferred that both treatments bring the alloy to closely equivalent states. This finding allows one to obtain valid interpolated values of A for Cu–15Al and Cu–10Al. With these values, and those of r_0, $A_2 (= Ar_0^2) = 8 \times 10^{-6}/6.7 \times 10^{-6}$ m^2 sec^{-1} for 15/10Al results.

It can be then concluded that A_2 is essentially insensitive to the alloy composition, so in the following an average value between the three calculated ones, $\bar{A}_2 = (7.5 \pm 0.8) \times 10^{-6}$ m^2 sec^{-1}, will be used. This result is not surprising. In fact, the concentration in the matrix at the precipitate–matrix interface c_1 is independent of the alloy composition $\bar{c}$ and also of T in this case, because it is assumed that the interface is always at the critical temperature T_c during the dissolution process [37]. T_c is quite insensitive to the aluminium content in an extensive range of $\bar{c}$ [25, 38].

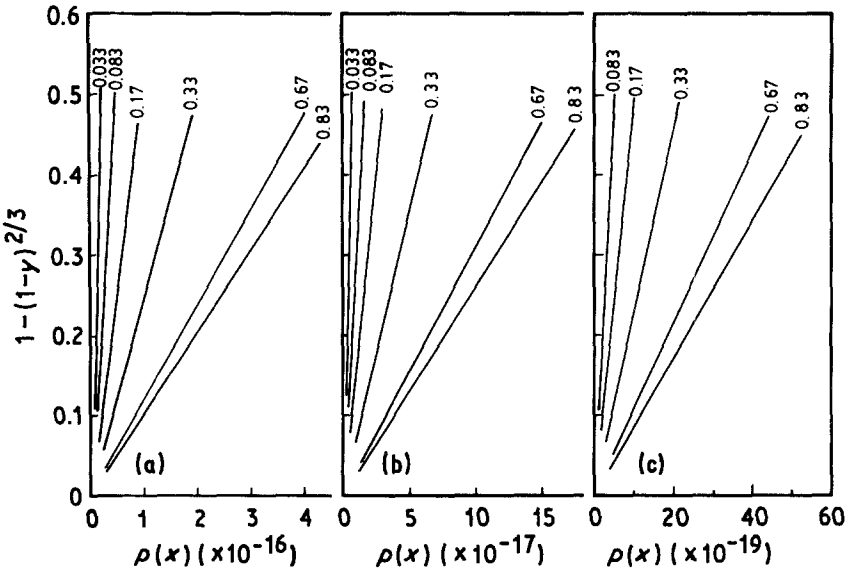

Figure 6 $1 - (1 - y)^{2/3}$ against $p(x)$ plots for the indicated heating rates α (K sec^{-1}). (a) Cu–19Al, (b) Cu–13Al, (c) Cu–6.5Al.

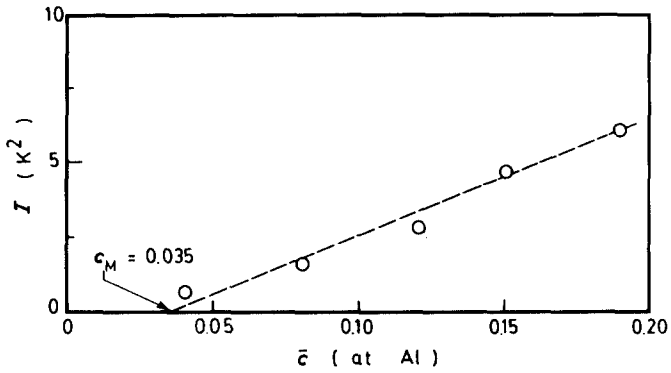

Figure 8 Area of DTA traces, I, against the alloy composition for α-Cu–Al alloys quenched from 723 K (data were obtained by processing Fig. 5 of [14]).

Also an equilibrium threshold value of $\bar{c}$ ($= c_M$) for disperse-order emergence of about 0.035, and a critical temperature $T_c(c_M) = 513$ K, can be estimated from the calorimetric data of Popplewell and Crane [14] in quenched alloys. The above estimation for c_M was made by extrapolating to zero the area of the disperse-order formation DTA traces plotted as a function of the alloy composition (Fig. 8). Since $T_c(c_M)$ is about the same as those corresponding to alloys with larger aluminium contents [25, 38], one may infer that c_M is essentially independent of T below T_c, constituting the lower equilibrium boundary for the (α + DO) field. Furthermore, the dissolution model leading to Equation 10 requires c_M to be considered at an arbitrary temperature below the equilibrium dissolution value [25] (usually room temperature is taken). On the other hand, $c_p = 0.228$ [35, 39], and an average value of $D_0 \simeq 6.45 \times 10^{-5}\,m^2\,sec^{-1}$ can be taken since, as will be shown later, D_0 is quite insensitive to $\bar{c}$. Therefore, from Section 2, it is permissible to set

$$A_2 = K_2 = 2[(c_I - c_M)/(c_p - c_I)]\,D_0 \quad (15)$$

which is simultaneously insensitive to T and, as was also found experimentally, to $\bar{c}$.

With the previously given values for c_M, c_p, D_0 and the above calculated value for $\bar{A}_2$, one obtains from Equation 15: $c_I = 0.046$, which is quite good, since it is somewhat larger than c_M and much smaller than c_p as is the case in practice [12].

By computing m for the different heating rates from Fig. 6, the domain sizes at the onset of the dissolution process can then be calculated for each alloy.

If r_0^3 is plotted against α, linear dependences are observed for α ranging from 0.033 to 0.83 K sec^{-1}, as shown in Fig. 9. For higher heating rates it becomes constant at r_c^3, as a consequence of a limiting value of supersaturation of disperse order retained from the freezing temperature. As dynamic equilibrium is reached for $\alpha = 0.033\,K\,sec^{-1}$ at $T < T_c(0.033)$ [25] the straight lines can be extrapolated to $\alpha = 0$, so a finite value $r_0^3(0) = r_c^3$ exists; hence r_c represents a critical radius. All these findings confirm, from the above kinetic analysis, that the order/disorder process is a first-order transition as already found on the basis of an enthalpimetric analysis [25], where the presence of an energy absorption above T_c (Stage 2), even under the dynamic equilibrium conditions of Stage 1, is indicative of such a feature. The above conclusion is furthermore in agreement with the fact that the transition occurs from a very highly heterogeneous ordered state (in the alloy containing 19 at % Al the volume fraction of particles reaches 0.6 [25]), based on the Cu_3Au superlattice structure LI_2 [20, 40, 41], to a homogeneous short-range order (SRO) state based on the CuAu superlattice LI_0 [42, 43]. The Landau rules [44] force the transition from $LI_2(Cu_3Au)$ to SRO to be first-order. Values for r_c and r_e are listed in Table II. One can appreciate, in agreement with the reported observations performed by TEM [35] and from Fig. 7 of the present work, that the domain radius increases with the aluminium content when compared at similar alloy states.

The effects of prolonged pre-anneals at 473 K is illustrated in the DSC traces appearing in Fig. 10 for Cu–19Al. The corresponding thermogram for the alloy heat-treated during 80 h is also shown for comparison. The outstanding displayed features are a slight decrease in the temperature interval of the trace as the annealing time becomes longer, together with an increase in the peak height. However, the peak temperature and the associated dissolution enthalpy

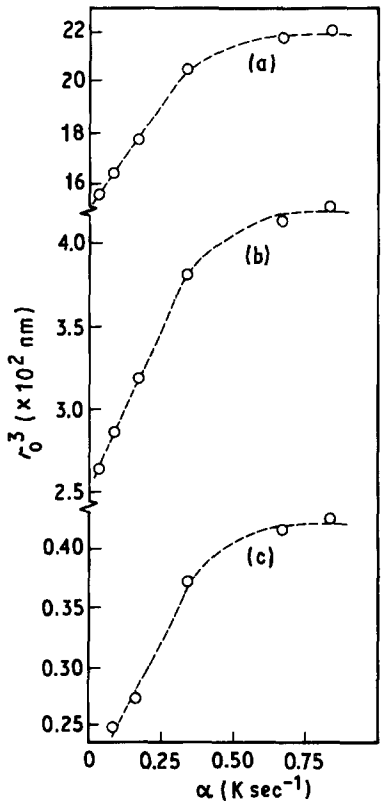

Figure 9 Calculated r_0^3 values as a function of the heating rate for α-Cu–Al alloys furnace-cooled at 15 K h^{-1} and subsequently pre-annealed for 80 h. (a) Cu–19Al, (b) Cu–13Al, (c) Cu–6.5Al.

TABLE II Compositional dependence of r_c and r_e*

Al (at %)	r_c (nm)	r_e (nm)
19	11.5 ± 0.4	13.0 ± 0.4
13	6.3 ± 0.3	7.5 ± 0.3
6.5	2.7 ± 0.2	3.5 ± 0.2

*Data represent the average of 5 runs.

remain unaltered. These results can be interpreted in terms of a particle distribution modification. In fact, one may expect that as the pre-annealing time increases, the distribution variance decreases and hence, since more particles reach sizes closer to the mean size, the individual precipitate dissolution takes place in a more similar temperature interval. Furthermore, a smaller (larger) pre-existing mean domain radius will be reflected in a lower (higher) peak temperature, respectively, because of the increased (decreased) surface-to-volume ratio [45]. Therefore, as the peak temperature and the dissolution enthalpy remained unchanged regardless of the annealing time and, since the DSC runs were carried out at the same heating rate (0.83 K sec^{-1}), it can be inferred both that the mean size and volume fraction were not altered, and that the shape differences displayed by DSC traces can be attributed to changes in particle distribution.

4.4. The domain concentration

An experimental procedure based on enthalpimetric measurements, and also on the previous kinetic analysis, was developed in order to estimate domain concentrations. In fact, as Stage 1 is suppressed for $\alpha = 0.83\ K\ sec^{-1}$ (Fig. 1), it can be supposed that such a heating rate is too high to develop this stage, merely for kinetic reasons. These features can be used in order to make a rough determination of N_e.

Samples cooled at 15 K h^{-1} were annealed at different temperatures, T_a, for 80 h and then heated at 0.83 K sec^{-1}. For the sake of brevity, in Fig. 11 DSC traces are shown only for the 19 at % Al alloy. The energy under the peaks, ΔH_e, was evaluated between $T_c(0.83)$ and $T_f(0.83)$. Values for T_a and those corresponding to ΔH_e are listed in Table III. It can be noticed that the heat absorbed below a certain annealing temperature remains constant, then it decreases as the annealing temperature increases. Large annealing times did not produce measurable changes in their values. Therefore, associated with each of these energies there is a disordering enthalpy characteristic of a state of order associated with a volume fraction, V_e, which is expected to be closer to equilibrium as the corresponding annealing temperature increases. It is worthwhile noticing that at T_c, $V_e = V_c$ should hold. Departure from equilibrium becomes important when the annealing temperature is low enough that the system becomes "frozen in". This feature is revealed by the steadiness in the measured values. A calibration factor β (= 377 J mol^{-1}) relating precipitate volume fraction and dissolution energy was previously computed [25], so V_e ($= \Delta H_e/\beta$) can be readily obtained. Its values appear in Table III.

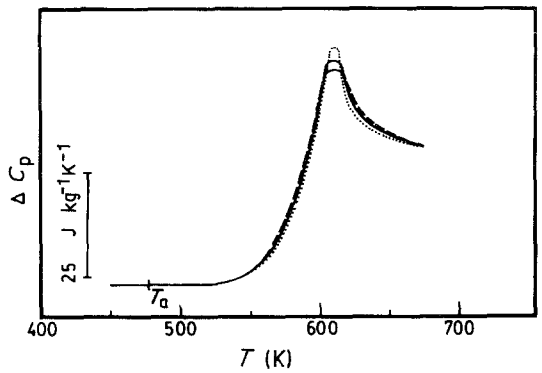

Figure 10 DSC thermograms for Cu–19Al obtained with a heating rate of 0.83 K sec^{-1} after annealing at T_a = 470 K for various times: (---) 80 h, (——) 240 h, (· · ·) 480 h.

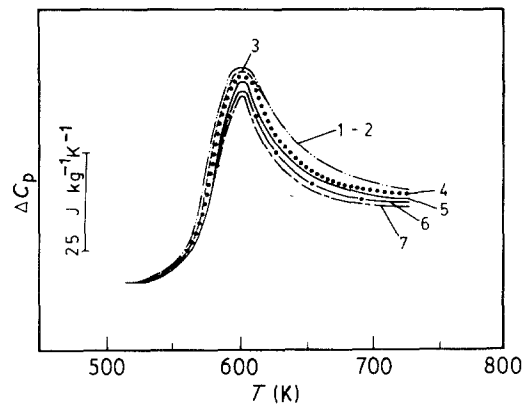

Figure 11 DSC thermograms for Cu–19Al with a heating rate 0.83 K sec^{-1} pre-annealed for 80 h at the following temperatures: (1) 353 K, (2) 373 K, (3) 423 K, (4) 473 K, (5) 500 K, (6) 510 K and (7) 515 K.

From the thermogram of Fig. 10 and those corresponding to the 13 and 6.5 at % Al displayed at the different annealing temperatures for $\alpha = 0.83$ K sec^{-1}, values for r_e can be determined using the same procedure described in Section 4.3. Since $V_e = (4/3)\pi N_e r_e^3$, the domain concentration N_e can readily be computed. Values for r_e and N_e are also listed in Table III.

It can be noticed that N_e decreases with the aluminium content while V_e increases. Because of the high concentration of aluminium in Cu–19Al, the volume fraction of the ordered regions reaches values as high as 0.6. This result, which was also found by Trieb and Veith [30] suggests that these regions nearly touch and form a structure of microdomains with antiphase boundaries (APB). Such a suggestion would also be favoured by the rather high precipitate–matrix specific interfacial energy (498 mJ m^{-2}) reported for Cu–19Al [46] which is larger than the usual values consistent with coherency [47]. (An improved value of 456 mJ m^{-2} was recently calculated [46].) Therefore, at high concentrations, a transition to a microdomain structure seems possible.

The dependence of particle number and size on temperature was explained qualitatively for Cu–18Al during isothermal annealing [30] with the help of a hypothetical microdomain model. In agreement with the present computations, it was concluded that de-coarsening together with a decrease of the number of regions N_e with increasing T_a will take place. The decrease of N_e with increasing T_a was also predicted

TABLE III Disperse-order dissolution enthalpy, volume fractions, radii and concentration for the indicated annealing temperatures computed from DSC traces obtained with $\alpha = 0.83\,K\,sec^{-1}$. The diffusion times ($t_{0.5}$) and the system "freezing" temperatures (T_z) are also indicated

Al (at %)	T_z (K)	T_a (K)	ΔH_e ($J\,mol^{-1}$)	V_e	$t_{0.5}$ (h)	r_e (mm)	N ($\times 10^{22}\,m^{-3}$)
19		353	226	0.60	3.3×10^6	13.0	6.52
		373	226	0.60	2.27×10^5	13.0	6.52
		423	220	0.58	9.93×10^2	12.87	6.50
	460	473	210	0.56	12.3	12.75	6.45
		500	193	0.51	2.2	12.50	6.23
		510	182	0.48 V_{eq}	1.2	12.34 r_{eq}	6.10 N_{eq}
		515	180	0.477	0.9	12.31	6.10
		(520) T_c				(12.15)	(6.05)
13		353	50	0.13	1.96×10^8	7.5	7.36
		373	50	0.13	8.9×10^6	7.5	7.36
		423	48	0.127	2.96×10^4	7.4	7.48
	470	473	46	0.12	3.54×10^2	7.3	7.36
		500	39	0.10	64.1	6.9	7.27
		510	35	0.09 V_{eq}	38.8	6.7 r_{eq}	7.14 N_{eq}
		520	31	0.08	24.7	6.5	6.95
		(535) T_c				(6.1)	(6.70)
6.5		373	5.8	0.015	9.4×10^{10}	3.5	8.57
		405	5.7	0.015	1.6×10^8	3.48	8.55
		445	5.6	0.015	1.3×10^7	3.46	8.51
	474	493	5.4	0.014	1.6×10^5	3.41	8.60
		520	5.1	0.0135	2.0×10^4	3.35	8.57
		525	4.9	0.013 V_{eq}	1.5×10^4	3.31	8.56
		530	4.7	0.0125	1.1×10^4	3.26	8.61
		(540) T_c				(3.1)	(8.57) av.

for Cu–15Al by Aubauer's theory [48] for the stability of coherent concentration modulations.

4.5. Equilibrium attainment

The next step will be concerned with the determination of equilibrium values (V_{eq}, N_{eq}, r_{eq}) for V_e and N_e, and hence for r_e. It is first worth recalling that equilibration of V_e will proceed relatively fast owing to the short-circuit diffusion of atoms between the particles and the surrounding matrix; thus equilibrium can be reached at lower annealing temperatures than those required to equilibrate N_e.

One criterion to determine the lower value of T_a for which V_e is in equilibrium (or very close to it) might consist in computing the temperature θ_1 which represents the equilibrium state of the alloy after annealing at T_a for 80 h. For equilibrium to be attained, θ_1 should come out not much higher than T_a (say 4 to 8 K) and of course always higher than T_z, the freezing system temperature. T_z was estimated for each alloy in previous work [25] from ΔH_e against T_a plots; its values are also shown in Table III.

Integration of the differential equation which describes the rate of approach to equilibrium given by Bragg and Williams (Equation 1 of [25]) leads to

$$\theta_1 = T_a + (\theta_0 - T_a) \exp [-t/\tau(T_a)] \quad (16)$$

where τ is the relaxation time obeying a relationship of the type $\tau = \tau_0 \exp (E/RT)$, τ_0 is a constant and E is the activation energy required for interchange of atomic positions already computed by the Kissinger method. In the present experiments the alloys were furnace-cooled at a rate of $15\,K\,h^{-1}$. Therefore a metastable value for V_e was reached at θ_0(Cu–19Al) = 494 K and θ_0(Cu–13Al) = 493 K calculated from Equation 14, taking τ_0 associated with this process equal to $3.49 \times 10^{-13}/2.06 \times 10^{-13}$ sec for 19/13 at % Al. Subsequently, they were annealed for 80 h at the indicated values of T_a in Table III. In Cu–19Al, $\theta_1 = 456$ K for $T_a = 423$ K, while at $T_a = 473$ K, $\theta_1 = 473$ K results. Therefore, V_e can be considered to be in equilibrium at a limiting value of T_a close to $T_z = 460$ K in practice. For Cu–13Al, $\theta_1 = 480$ K when $T_a = 473$ K, thus a value close to $T_a = 470$ K was taken in this case. Such computations were not made for Cu–6.5Al because τ_0 was not available, and hence the limiting value of T_a was simply taken at $T_z = 474$ K in view of the results obtained before. In Table III the arrows indicate the range of V_{eq}. It is worth noticing that in the ranges referred to one finds $\theta_1 < T_a$, thus ensuring equilibration.

The adjustment to equilibrium of a new number of precipitated domains requires a different criterion for evaluating the limiting value of T_a, since here atoms must diffuse between the precipitate regions themselves, which corresponds to longer diffusion paths. Therefore it is expected that N_e would "freeze" at higher temperatures than V_e. Whether or not diffusion has taken place between domains will depend on the value of the diffusion time at the annealing temperature, $t_{0.5}(T_a)$. Since, as pointed out before, larger annealing times did not produce measurable changes in ΔH_e, the following criterion seems reasonable in order to decide on it: if this time is shorter or comparable to 80 h, atoms have diffused between the precipitate regions and N_e can attain its equilibrium value. On the other hand, N_e remains "frozen in" and the measured changes in ΔH_e must be associated with the tendency of the system to equilibrate only V_e to the imposed value of T_a.

The diffusion time can be easily estimated as

$$t_{0.5}(T_a) = \frac{4}{9D_0}\left(\frac{r_e}{V_e}\right)^2 \exp\left(\frac{E}{RT_a}\right) \quad (17)$$

where D_0 is the diffusion constant and E the interdiffusion activation energy. D_0 was computed [49] from

$$D_0 = D_{00}\left[kT_m(\bar{c})\frac{a^2(\bar{c})}{M(\bar{c})}\right]^{1/2} \quad (18)$$

Here $D_{00} = 400$ for f c c structures [50], k is the Boltzmann constant, $T_m(\bar{c})$ is a characteristic temperature which is equal to the mean line of the solidus and liquidus, $a(\bar{c})$ is the lattice parameter of the alloy and $M(\bar{c})$ the mass of the "average" AB atom given by the expression

$$\frac{1}{M(\bar{c})} = \frac{\bar{c}}{M_{Al}} + \frac{(1-\bar{c})}{M_{Cu}} \quad (19)$$

From the Cu–Al equilibrium diagram, values for $T_M(\bar{c})$ of 1313/1323/1348 K were measured for 19/13/6.5 at % Al, while the corresponding computed values for $M(\bar{c})$ and $a(\bar{c})$ were $9.4 \times 10^{-26}/9.73 \times 10^{-26}/1.02 \times 10^{-25}$ kg per atom and $3.69 \times 10^{-10}/3.67 \times 10^{-10}/3.64 \times 10^{-10}$ m, respectively. When D_0 is computed by the above procedure, one obtains $6.68 \times 10^{-5}/6.45 \times 10^{-5}/6.22 \times 10^{-5}$ m^{2}sec^{-1} for 19/13/6.5 at % Al. With the values for r_e, V_e and E already computed, $t_{0.5}(T_a)$ was determined. Its values also appear in Table III. The corresponding range for N_{eq} (and hence r_{eq}) resulting from the application of the above criterion is indicated by the respective arrows, showing also that N_e "freezes" at somewhat higher values of T_a than V_e, as expected. However, since for Cu–6.5Al N_e remains constant regardless of T_a, and as the diffusion time is about 10^4 h even close to the critical temperature, it is unlikely that equilibrium can be attained in a reasonable time of annealing. These results suggest that the ordering process for this alloy composition is probably associated with short-range order rather than dispersed order. On the other hand, they might be interpreted on the basis that a disperse-ordered state exists, but equilibration of the domain concentration is not allowed to be attained merely for kinetic reasons. The existence of an order–disorder critical temperature almost equal to those corresponding to alloys with a higher aluminium content is in support of the latter interpretation. However, no final conclusion can be drawn, and combined TEM–DSC work is needed for such diluted alloys.

Epperson *et al.* [51] reported that it is unsafe to apply the X-ray diffuse scattering technique for detecting SRO if the alloys contain less than about 5 or 6 at % Al. This seems to explain why Scattergood *et al.* [52], using this technique, predicted the existence of an order–disorder phase boundary at about 6 at % Al. The present DSC experiments confirm that this boundary lies below that alloy composition, in agreement with the processed DTA data of Popplewell and Crane [14] from which one can predict it (as shown in Fig. 8) at about 3.5 at % Al. We believe, however, that, for pre-annealed alloys it lies at a somewhat larger percentage of aluminium, since the above value is based on order development after quenching. Such conditions give rise to larger volume fractions than those corresponding to equilibrium, because of the enhanced nucleation which is assisted by the quenched-in defects. This feature was shown in previous work by the high values of N_e computed [23].

For diluted alloys approaching the threshold concentration, it can be inferred from the present study that V_e vanishes via r_e, since N_e was found to increase as the aluminium content decreases. Therefore, it is likely that the heterogeneity of the microstructure would still be justified, though, in a wider sense than highly ordered particles in a highly disordered matrix. The consideration of concentration fluctuations in addition to the statistical concept of SRO can account for the onset of disperse-order formation. Such a consideration was used recently by Trattner and Pfeilner [53] and by Pfeiler *et al.* [54] for explaining relaxation behaviour in alloys which do not follow a single exponential process [34, 48, 55].

In closing, all the computed data are represented semi-quantitatively in an r_e–N_e–T plot for the three alloy compositions in Fig. 12. On the surface EFGH there lie the values for r_{eq} where the system is in equilibrium, while on the surface HIJK only V_e is in equilibrium outside EFGH. FG and JK represent the concentration limits for the system and volume fraction equilibrium attainment, respectively. The point L accounts for a transition from DO to a heterogeneous structure based on concentration fluctuations or simply to SRO, and hence represents the limit between particle dissolution by a first- or a second-order transition. The freezing boundaries for the domain number EF and for the whole system IJ, based on T_z, are also indicated. The critical boundary HGKL is associated with the critical temperature. Finally, a threshold concentration for deviation of alloy atoms from a random distribution is also indicated.

5. Conclusions

The investigation by differential scanning calorimetry (DSC) on the disordering kinetics in pre-annealed α-Cu–Al alloys leads to the following conclusions:

(a) The dissolution kinetics of ordered domains in α-Cu–Al alloys can be quite well described by a kinetic model function in the integrated form $f(y) = 1 - (1 - y)^{2/3}$.

(b) By performing DSC runs at different heating rates, the model allowed us to compute the domain sizes corresponding to the pre-annealed state and also to estimate their critical values. The existence of critical radii indicates that the dissolution process occurs by a first-order transition, as previously reported.

(c) After pre-annealing the alloys at different temperatures, domain sizes and volume fractions, computed from dissolution kinetics under high heating rate conditions and enthalpimetric determinations, respectively, revealed that the volume fraction decreases as the temperature increases, while the contrary occurs for the domain number. In addition, as the aluminium content increases the volume fraction also does so; in the mean time, the domain concentration decreases.

(d) With the above pre-anneals, it was possible to

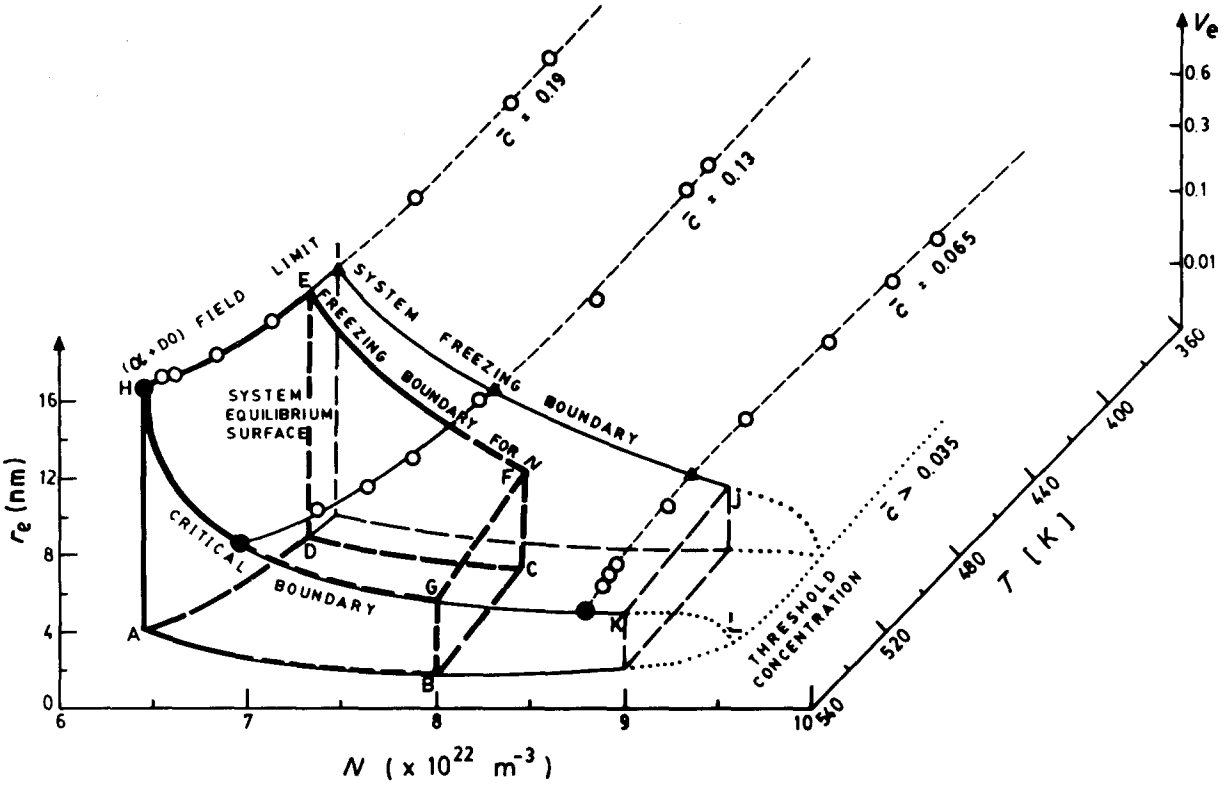

Figure 12 A representation of the domain size–domain concentration–temperature interdependence. The volume fraction axis is also indicated. (●) T_c, (▲) T_z.

estimate on the basis of appropriate time constants and diffusion times the range of temperatures compatible with volume fraction and domain number equilibrium attainment.

(e) Prolonged pre-anneals indicate, from DSC data analysis, that the particle distribution becomes sharper, although the mean domain size and volume fraction remain unaltered.

(f) From the computed data, a semi-quantitative r_e–N_e–T diagram is proposed for α-Cu–Al alloys, where different zones and boundaries characterizing the disperse-ordered domains are delineated.

Acknowledgements

The authors wish to thank the Departamento de Investigación y Bibliotecas de la Universidad de Chile (Contract I. 2294.8625) and the Fondo Nacional de Desarrollo Científico y Tecnológico (Contract No. 6001/85) for financial support. They are also indebted to the Instituto de Investgaciones y Ensayes de Materiales, Facultad de Ciencias Físicas y Matemáticas, Universidad de Chile for financial support and for the facilities given for this research.

References

1. E. LANG, *Z. Metallkde* **64** (1973) 56.
2. R. DE IASI and P. N. ADLER, *Metall. Trans.* **8A** (1977) 1177.
3. P. N. ADLER and R. DE IASI, *ibid.* **8A** (1977) 1185.
4. B. MAILLARD, J. J. VILLENEVE and C. FILLIATRE, *Thermochim. Acta* **33** (1979) 107.
5. J. M. PAPAZIAN, *Metall. Trans.* **12A** (1981) 269.
6. *Idem, ibid.* **13A** (1982) 761.
7. R. J. LITVAK and J. M. PAPAZIAN, *Scripta Metall.* **18** (1984) 483.
8. E. S. BALMUTH, *ibid.* **18** (1984) 301.
9. D. DOLLIMOR, in "The State-of-the-Art of Thermal Analysis", edited by O. Menis, H. Rock and P. D. Garn, NBS Special Publication No. 580 (US Government Printing Office, Washington, DC, 1980) p. 1.
10. M. E. BROWN and C. A. R. PHILLPOTTS, *J. of Chem. Educ.* **55** (1978) 556.
11. P. D. GARN, *Crit. Rev. Anal. Chem.* **3** (1972) 65.
12. M. J. WHELAN, *Met. Sci. J.* **3** (1969) 65.
13. A. VARSCHAVSKY and E. DONOSO, *Thermochim. Acta* **69** (1983) 34.
14. J. M. POPPLEWELL and J. CRANE, *Metall. Trans.* **2** (1971) 3411.
15. C. KONOSHITA, Y. TOMOKIYO, H. MATSUDA and T. EGUCHI, *Trans. Jpn Inst. Met.* **14** (1973) 91.
16. E. DONOSO and A. VARSCHAVSKY, *Mater. Sci. Engng.* **37** (1979) 151.
17. V. Y. PANIN, E. K. ZENKOVA and V. P. FADIN, *Phys. Metall. Metalloved.* **13** (1962) 85.
18. C. R. BROOKS and E. E. STANSBURY, *Acta Metall.* **11** (1963) 1303.
19. S. MATSUO and L. M. CLAREBROUGH, *ibid.* **11** (1963) 1195.
20. Y. TOMOKIYO, N. KUWANO and T. EGUCHI, *Trans. Jpn Inst. Met.* **16** (1975) 489.
21. J. M. ROLAND, X. QUILLARD and A. MOREAU, *Phys. Status Solidi (a)* **64** (1981) 45.
22. A. VARSCHAVSKY, *Metall. Trans.* **13A** (1982) 801.
23. A. VARSCHAVSKY and E. DONOSO, *ibid.* **14A** (1983) 875.
24. K. G. GUPTA, T. R. RAMACHANDRAN, K. P. RAJENDRAN and S. DAS, *J. Mater. Sci. Lett.* **3** (1984) 100.
25. A. VARSCHAVSKY and E. DONOSO, *Metall. Trans.* **15A** (1984) 1999.
26. C. D. DOYLE, *Nature* **207** (1965) 290.
27. T. OZAWA, *J. Therm. Anal.* **9** (1976) 369.
28. H. S. CARSLAW and J. C. JAEGER, "Conduction of Heat in Solids", 2nd Edn (Claredon Press, Oxford, 1959) p. 247.
29. A. TORREJÓN and M. I. PÉREZ, *J. Phys. E* **6** (1973) 810.
30. L. TRIEB and G. VEITH, *Acta Metall.* **26** (1978) 185.
31. H. E. KISSINGER, *Anal. Chem.* **28** (1957) 1702.
32. G. VEITH, L. TRIEB, W. PUSCHL and H. P. AUBAUER, *Phys. Status Solidi* **27** (1975) 59.

33. B. G. CHILDS and A. D. LE CLAIRE, *Acta Metall.* **2** (1954) 718.
34. C. Y. LI and A. S. NOWICK, *Phys. Rev.* **103** (1956) 294.
35. W. GAUDIG and H. WARLIMONT, *Z. Metallkde* **60** (1969) 488.
36. W. R. BRAGG and E. J. WILLIAMS, *Proc. R. Soc.* **145A** (1934) 699.
37. H. B. AARON, D. FAINSTEIN and G. R. KOTLER, *J. Appl. Phys.* **41** (1970) 4404.
38. W. GAUDIG, P. OKAMOTO, G. SCHANZ, G. THOMAS and H. WARLIMONT, in Proceedings of 3rd Bolton Landing Conference, September 1969 (Claitor, Baton Rogue, Louisiana, 1970) p. 347.
39. M. ZEHETBAUER, L. TRIEB and H. P. AUBAUER, *Z. Metallkde* **67** (1976) 431.
40. W. GAUDING and H. WARLIMONT, *Acta Metall.* **26** (1978) 709.
41. A. VARSCHAVSKY, M. I. PÉREZ and T. LOBEL, *Metall. Trans.* **6A** (1975) 577.
42. A. GOYAL, S. K. SI and K. P. GUPTA, *Scripta Metall.* **9** (1975) 23.
43. B. W. ROBERTO, *Acta Metall.* **2** (1954) 597.
44. L. D. LANDAU and E. M. LIFSHITZ, "Statistical Physics" (Addison-Wesley, Reading, Massachusetts, 1958).
45. P. G. SHEWMON, "Transformations in Metals", 1st Edn (McGraw-Hill, New York, 1969) p. 150.
46. A. VARSCHAVSKY, *J. Mater. Sci.* **20** (1985) 3881.
47. J. D. BOYD and R. B. NICHOLSON, *Acta Metall.* **19** (1971) 1101.
48. H. P. AUBAUER, *Phys. Status Solidi (a)* **43** (1977) 601.
49. D. L. BEKE, I. UZONYI and F. J. KEDVES, *Phil. Mag.* **A44** (1981) 983.
50. D. L. BEKE, G. ERDÉLYI and F. J. KEDVES, *J. Phys. Chem. Solids* **42** (1981) 163.
51. J. E. EPPERSON, P. FURNROHR and C. ORTIZ, *Acta Crystallogr.* **A34** (1978) 667.
52. R. O. SCATTERGOOD, S. C. MOSS and M. B. BEVER, *Acta Metall.* **18** (1970) 1087.
53. D. TRATTNER and W. PFEILER, *J. Phys. F* **13** (1983) 739.
54. W. PFEILER, R. REIHSNER and D. TRATTNER, *Scripta Metall.* **19** (1985) 199.
55. F. ADUNKA, L. TRIEB and M. ZEHETBAUER, *Phys. Status Solidi (a)* **62** (1980) 213.

Received 25 November 1985
and accepted 17 January 1986